PHYSICAL REVIEW D **91,** 035022 (2015)

Higgsino dark matter in nonuniversal gaugino mass models

Manimala Chakraborti,[1,*] Utpal Chattopadhyay,[1,†] Soumya Rao,[2,‡] and D. P. Roy[3,§]

[1]*Department of Theoretical Physics, Indian Association for the Cultivation of Science, 2A & B Raja S.C. Mullick Road, Jadavpur, Kolkata 700 032, India*

[2]*ARC Centre of Excellence for Particle Physics at the Terascale, School of Chemistry & Physics, University of Adelaide, Adelaide, SA 5005, Australia*

[3]*Homi Bhabha Centre for Science Education, Tata Institute of Fundamental Research, Mumbai 400088, India*

(Received 26 November 2014; published 19 February 2015)

We study two simple and well-motivated nonuniversal gaugino mass models, which predict Higgsino dark matter. One can account for the observed dark matter relic density along with the observed Higgs boson mass of $\simeq$125 GeV over a large region of the parameter space of each model, corresponding to a Higgsino mass of $\simeq$1 TeV. In each case this parameter region covers the gluino mass range of 2–3 TeV, parts of which can be probed by the 14 TeV LHC experiments. We study these model predictions for the LHC in brief and for dark matter detection experiments in greater detail.

DOI: 10.1103/PhysRevD.91.035022 PACS numbers: 12.60.Jv, 04.65.+e, 95.30.Cq

I. INTRODUCTION

Supersymmetry, in particular the minimal supersymmetric Standard Model (MSSM) [1–3], offers a natural candidate for the dark matter [4,5] of the Universe in the form of the lightest supersymmetric particle (LSP). Astrophysical constraints require it to be a colorless and neutral particle, while direct-detection experiments disfavor a sneutrino dark matter [6]. Thus the favored dark matter (DM) candidate in the MSSM is the lightest neutralino $\tilde{\chi}_1^0$ which could be any combination of the neutral gauginos, like the bino ($\tilde{B}$), wino ($\tilde{W}$), and Higgsinos $\tilde{H}_D$, $\tilde{H}_U$, i.e.,

$$\tilde{\chi}_1^0 = N_{11}\widetilde{B} + N_{12}\widetilde{W} + N_{13}\widetilde{H}_D + N_{14}\widetilde{H}_U. \qquad (1)$$

Here N_{ij} for $i, j = 1-4$ refers to elements of the matrix that diagonalizes the neutralino mass matrix [3].

In the simplest version of this model—called the constrained MSSM (CMSSM) or the minimal supergravity (mSUGRA) model [3,7]—the lightest neutralino as a dark matter candidate [4,5] is dominantly a bino over most of the parameter space. Since a bino does not carry any gauge charge, its main annihilation mechanism is the so-called bulk annihilation process via sfermion exchange. But the Higgs boson mass bound of 114 GeV from LEP [8] implied large sfermion masses in this model [9], which was reinforced with discovery of the Higgs boson at the LHC with a mass of about 125 GeV [10]. This implies a very inefficient bulk annihilation process, resulting in an overabundance of the dark matter relic density over most of the parameter space. We shall see below that there are only a few strips of parameter space available in the CMSSM giving a cosmologically compatible dark matter relic density—i.e., the stau coannihilation, the resonant annihilation, the focus point, and the Higgsino dark matter regions [3,11]—each of which requires some amount of fine-tuning between SUSY parameters. Moreover, large parts of the stau coannihilation and the resonant annihilation regions are disfavored by the Higgs boson mass of about 125 GeV, while most of the hyperbolic branch [11,12]/focus point [13] region is disfavored by the recent direct dark matter detection experiments [14]. While the Higgsino dark matter region is unaffected by these results, it corresponds to squark and gluino masses $\gtrsim$8–10 TeV in this model, which cannot be probed at the LHC [14,15]. Therefore this region has little practical interest at least for LHC experiments.

In this work we shall study the phenomenology of Higgsino dark matter in some simple and predictive nonuniversal gaugino mass (NUGM) models based on the SU(5) grand unified theory (GUT) [16–24]. The gaugino mass term in the GUT scale Lagrangian is bilinear in the gaugino fields, which belongs to the adjoint representation of the GUT group. Thus for the 24-dimensional representation of SU(5) the above must transform like one of the representations[1] occurring in their symmetric product [22]:

$$(24 \times 24)_{\text{symm}} = 1 + 24 + 75 + 200 \qquad (2)$$

The mSUGRA model considers the singlet representation for the gaugino mass term, implying a universal gaugino mass at the GUT scale. On the other hand, any of the three nonsinglet representations implies nonuniversal

*tpmc@iacs.res.in
†tpuc@iacs.res.in
‡soumya.rao@adelaide.edu.au
§dproy1@gmail.com

[1]Or a linear combination of them.

gaugino masses at the same scale. Each of these three NUGM models is as predictive as the CMSSM. We shall see below that the 24 model predicts a bino-dominated dark matter, as in the case of the CMSSM. But the 75 and the 200 models predict Higgsino-dominated dark matter over the bulk of their parameter spaces. Thus one can obtain the right amount of dark matter relic density by considering a Higgsino mass of ∼1 TeV [11,24]. Unlike the CMSSM, however, this is achieved here naturally with a significantly reduced degree of fine-tuning between SUSY parameters [25]. Moreover, for both these NUGM models, the cosmologically compatible relic density regions of Higgsino dark matter correspond to a gluino mass range of 2–3 TeV, at least a part of which can be probed by the 14 TeV LHC experiments. Therefore these nonuniversal gaugino mass models should be of great phenomenological interest in the near future.

In Sec. II we give a brief overview of the above-mentioned universal and nonuniversal gaugino mass models. In Sec. III we summarize the phenomenology of the dark matter relic density compatible regions of the CMSSM. In Sec. IV we describe the dark matter relic density compatible regions of the 75 model along with the Higgs boson mass constraint. We list the SUSY mass spectra for a set of benchmark points satisfying these constraints, which are expected to be within the reach of the 14 TeV LHC experiments. We also show the size of the gluino pair-production cross section for these points at the 14 TeV LHC and briefly discusses the signal characteristics. Then we compare the predictions of this model for various direct and indirect dark matter detection experiments. In Sec. V we give the analogous description for the 200 model. We conclude with a summary of our results in Sec. VI.

II. NONUNIVERSALITY OF GAUGINO MASSES IN SU(5) GUT

The gauge kinetic function that relates to the gaugino masses at the GUT scale originates from the vacuum expectation value of the F-term of a chiral superfield Φ which causes SUSY breaking. Thus the gaugino masses are obtained via a nonrenormalizable dimension-five operator as given below [22]:

$$L \supset \frac{\langle F_\Phi \rangle_{ij}}{M_{\rm Planck}} \lambda_i \lambda_j. \tag{3}$$

Here $\lambda_{1,2,3}$ are the U(1), SU(2), and SU(3) gaugino fields (bino, wino, and gluino, respectively). Since gauginos belong to the adjoint representation of the GUT group, Φ and F_Φ can belong to any of the irreducible representations occurring in their symmetric product [Eq. (2)], i.e., 1, 24, 75, or 200. Thus the unification scale gaugino masses for a given representation n of the SUSY-breaking superfield are determined in terms of one mass parameter $m^n_{1/2}$ as

TABLE I. Coefficients $C^n_{1,2,3}$ for the unification scale gaugino mass parameters for each representation.

n	C^n_3	C^n_2	C^n_1
1	1	1	1
24	1	−3/2	−1/2
75	1	3	−5
200	1	2	10

$$M^G_{1,2,3} = C^n_{1,2,3} m^n_{1/2}, \tag{4}$$

where the values of the coefficients $C^n_{1,2,3}$ are listed in Table I [16]. The coefficients C^n_3 are conventionally normalized to 1.

The CMSSM assumes the SUSY-breaking superfield Φ to be a singlet, implying universal gaugino masses at the GUT scale. On the other hand, any of the three nonsinglet representations of Φ would imply nonuniversal gaugino masses as per Table I. These nonuniversal gaugino mass models can be consistent with the universality of gauge couplings,[2] $\alpha_G \simeq 1/25$, and their phenomenology has been widely studied [16–24]. The superparticle masses at the electroweak scale are related to these GUT-scale gaugino masses along with the universal scalar mass parameter m_0 and trilinear coupling parameter A_0, via renormalization group equations (RGE). In particular, the gaugino masses evolve like the corresponding gauge couplings at the one-loop level of the RGE, implying

$$\begin{aligned} M_1 &= (\alpha_1/\alpha_G) M^G_1 \simeq (25/60) C^n_1 m^n_{1/2}, \\ M_2 &= (\alpha_2/\alpha_G) M^G_2 \simeq (25/30) C^n_2 m^n_{1/2}, \\ M_3 &= (\alpha_3/\alpha_G) M^G_3 \simeq (25/9) C^n_3 m^n_{1/2}. \end{aligned} \tag{5}$$

The corresponding Higgsino mass μ is obtained from the electroweak symmetry-breaking condition along with the RGE for the Higgs scalar masses. Neglecting contributions from the trilinear soft terms, one has a relatively simple expression for the Higgsino mass at the one-loop level of the RGE [26], i.e.,

$$\begin{aligned} \mu^2 + \frac{1}{2} M_Z^2 \simeq & -0.1 m_0^2 + 2.1 M_3^{G2} - 0.22 M_2^{G2} \\ & - 0.006 M_1^{G2} + 0.006 M_1^G M_2^G \\ & + 0.19 M_2^G M_3^G + 0.03 M_1^G M_3^G, \end{aligned} \tag{6}$$

where the numerical coefficients on the right-hand side correspond to a representative value of $\tan\beta = 10$, but have only modest variations over the moderate $\tan\beta$ region.

Our results are based on exact numerical solutions of the two-loop RGEs including also the contributions from the

[2]See Ref. [18] and references therein.

trilinear couplings using the SUSPECT code [27]. Nevertheless, the approximate formulas of Eqs. (5) and (6) are very useful in understanding the composition of the LSP dark matter in these models. The dominant contribution to the mass of the Higgsino (6) comes from the M_3^G term, implying $\mu \sim \sqrt{2} m_{1/2}$ from Table I for all four models. On the other hand, for the mass of the bino, Eq. (5) shows that $M_1 \sim 0.4 m_{1/2}$ for the CMSSM, implying a bino-dominated LSP dark matter in this model. One sees from Table I that M_1 is further suppressed by a factor of one half in the 24 model, implying an even more strongly bino-dominated LSP dark matter. Thus one obtains a generic overabundance of dark matter in the CMSSM as well as in the 24 model. For the 75 and the 200 models, however, one sees from Table I that the bino mass M_1 is enhanced by factors of 5 and 10, respectively, relative to the CMSSM, implying a Higgsino-dominated LSP dark matter in these nonuniversal gaugino mass models. Since the Higgsino has an efficient annihilation mechanism via its isospin gauge coupling to the W boson, one obtains a cosmologically compatible dark matter relic density in these models and this corresponds to a Higgsino mass $\mu \simeq 1$ TeV [11,24].

III. COSMOLOGICALLY COMPATIBLE DARK MATTER RELIC DENSITY REGIONS OF THE CMSSM

The cosmologically compatible dark matter relic density regions of the CMSSM have been thoroughly investigated over the last two years in light of the 125 GeV Higgs boson mass and other LHC results, as well as by taking into account the constraints from dark matter direct-detection experiments [14,15]. We shall briefly revisit this issue here as a prelude to our investigation of Higgsino dark matter in nonuniversal gaugino mass models. This will provide a very useful backdrop for comparing the relative advantage of the dark matter scenario in the latter models. We have used the SUSPECT [27] code in our computation which uses two-loop RGEs and radiative electroweak symmetry breaking (REWSB) to generate the electroweak scale SUSY spectra. We consider a theoretical uncertainty of around 3 GeV in the lightest Higgs scalar mass m_h within the MSSM. This arises due to the EWSB scale dependence, the renormalization scheme (such as the $\overline{DR}$ or the on-shell schemes as used in SUSPECT and FEYNHIGGS [28], respectively), uncertainties in the mass of the top quark, and higher-order loop corrections up to three loops [29]. Hence, we assume that a mass of 122 GeV should be consistent with the Higgs data.

Figure 1 shows the CMSSM parameter space for representative values of moderate $\tan\beta$ [$= 10$, Fig. 1(a)] and large $\tan\beta$ [$= 50$, Fig. 1(b)]. The shaded region on top is disallowed due to the lack of REWSB ($\mu^2 < 0$), while the bottom strip is disallowed because the stau becomes the LSP. The constraints from the Higgs boson mass band of 122–125 GeV are indicated by the blue solid lines. Note that one requires a fairly large value of the GUT scale trilinear coupling parameter, $A_0 = -2$ TeV, consistent with the charge and color breaking constraint [30] to raise the Higgs mass above 122 GeV via the top-squark mixing contribution at $\tan\beta = 10$. The constraints from the $B_s \to \mu^+\mu^-(2\sigma)$ [31–34] and $b \to s\gamma(3\sigma)$ [35,36] decays are also indicated:

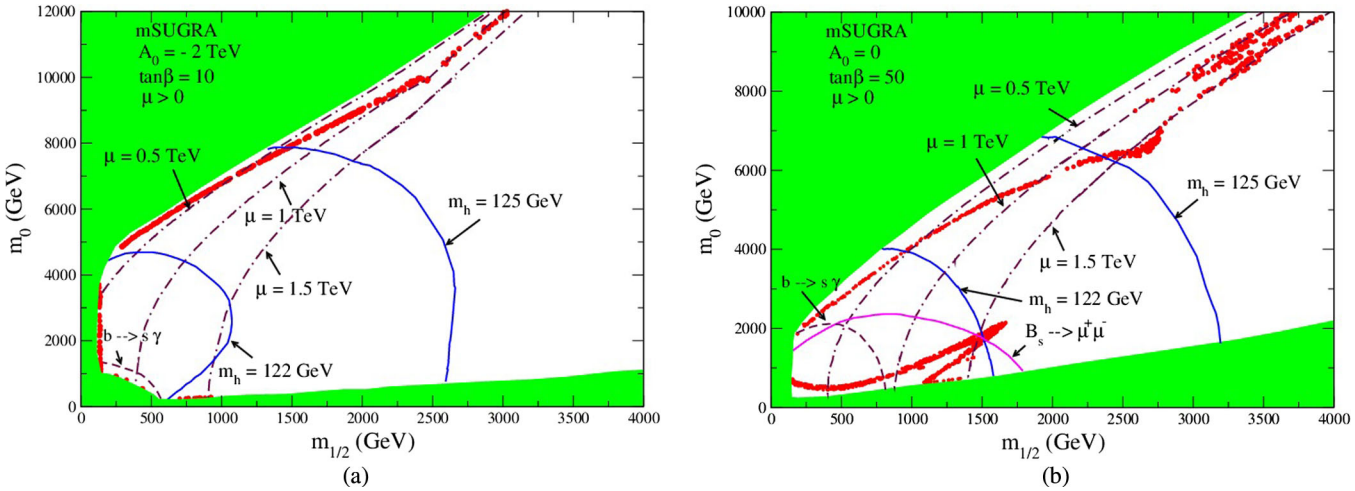

FIG. 1 (color online). The CMSSM/mSUGRA parameter space for representative values of moderate $\tan\beta = 10$ (a) and large $\tan\beta = 50$ (b). The cosmologically compatible dark matter relic density regions are indicated by the red dots, while the constraints from the Higgs boson mass band of 122–125 GeV are indicated by the blue solid lines. The constraints from $B_s \to \mu^+\mu^-$ and $b \to s\gamma$ decays are also indicated by solid magenta and maroon dashed lines, respectively (see text). The region above these lines is allowed by the corresponding constraints. The green region at the top is mostly excluded due to absence of REWSB (μ^2 turning negative), while the green region at the bottom is excluded because of the stau becoming the LSP.

$$2.77 \times 10^{-4} < \mathrm{Br}(b \to s\gamma) < 4.09 \times 10^{-4},$$
$$0.67 \times 10^{-9} < \mathrm{Br}(B_s \to \mu^+\mu^-) < 6.22 \times 10^{-9}. \quad (7)$$

The strips of red dots indicate the cosmologically compatible dark matter relic density regions, satisfying WMAP [37]/ Planck [38] data,[3]

$$0.09 < \Omega h^2 < 0.14. \quad (8)$$

They are usually classified into the following four regions.[4]

(1) The stau coannihilation region is the short strip adjacent to the lower boundary in Fig. 1(a), where the LSP dark matter coannihilates with a nearly degenerate stau, $\tilde{\chi}_1^0\tilde{\tau}_1 \to \tau\gamma(Z)$, via s-channel τ or t-channel $\tilde{\tau}$ exchange. It requires a degeneracy between the bino dark matter and the stau masses to within 10%–15%.

(2) The resonant annihilation region is the funnel-shaped strip in Fig. 1(b), corresponding to s-channel annihilation of the dark matter pair into a fermion pair $\tilde{\chi}_1^0\tilde{\chi}_1^0 \to f\bar{f}$ principally via the pseudoscalar Higgs boson A.

Since the $H\tilde{\chi}_1^0\tilde{\chi}_1^0$ and $A\tilde{\chi}_1^0\tilde{\chi}_1^0$ couplings are proportional to the product of the gaugino and Higgsino components of $\tilde{\chi}_1^0$ the same are strongly suppressed for a bino-dominated LSP. Therefore it requires the resonance condition, $M_A \simeq 2M_1$, for enhancement from the Breit-Wigner denominator along with a large $\tan\beta$ for a large coupling of A to the fermion pair. Note that both the stau coannihilation and resonant annihilation regions require some fine-tuning between independent SUSY mass parameters. Besides, large parts of both regions are disfavored by the Higgs boson mass constraint.

(3) The hyperbolic branch/focus point region near the upper boundary in each part of Fig. 1 extends up to $m_{1/2} \simeq 3$ TeV. Here the LSP has a large admixture of bino and Higgsino components because $\mu \sim M_1$. Since the $Z\tilde{\chi}_1^0\,\tilde{\chi}_1^0$ coupling is proportional to the difference of the squares of the Higgsino components of $\tilde{\chi}_1^0$ (i.e., $N_{13}^2 - N_{14}^2$), the pair annihilation $\tilde{\chi}_1^0\tilde{\chi}_1^0 \to f\bar{f}$ occurs mainly via Z-boson exchange.

By rewriting the electroweak symmetry-breaking condition [Eq. (6)] for the CMSSM in terms of m_0 and $m_{1/2}$ one obtains the hyperbolic equation in $m_{1/2}$ and m_0 for fixed values of μ,

$$\mu^2 + \frac{1}{2}M_Z^2 \simeq -0.1m_0^2 + 2m_{1/2}^2. \quad (9)$$

One can have a substantial cancellation between the two terms on the right-hand side, within the hyperbolic branch/focus point region with $m_0 \gg m_{1/2}$. This ensures a low value of $\mu \sim M_1 \sim 0.4m_{1/2}$. Note, however, that it implies a significant amount of fine-tuning between m_0 and $m_{1/2}$. Moreover, most of this region is strongly disfavored by the negative results from the recent DM direct detection experiments [14]. The reason is that sizable gaugino and Higgsino components of $\tilde{\chi}_1^0$ in this region imply a large $H\tilde{\chi}_1^0\,\tilde{\chi}_1^0$ coupling, predicting a large spin-independent (SI) $\tilde{\chi}_1^0 p$ cross sections for these experiments.

(4) Finally, the right end of the strip near the upper boundary corresponds to $\mu \lesssim M_1$, i.e., $\mu \lesssim 0.4m_{1/2}$, implying a Higgsino-dominated dark matter in the CMSSM [11]. Since the Higgsino pair can annihilate via their gauge coupling to W bosons, one obtains the desired dark matter relic density [Eq. (8)] for a Higgsino DM mass $\mu \simeq 1$ TeV, practically independent of any other SUSY parameter. The Higgsino DM region is realized for $m_{1/2} \gtrsim 3$ TeV so that the mass of the bino $M_1 \gtrsim 1.2$ TeV [Eq. (5)], while the corresponding gluino mass is above 10 TeV. The squark masses are also sufficiently heavy, which implies that the strongly interacting sparticles are well beyond the reach of the LHC at 14 TeV. The TeV scale superparticle masses can nevertheless easily account for the desired Higgs boson mass of ∼125 GeV. However, one sees from the above hyperbolic equation [Eq. (9)] that in this case there is at least as large a fine-tuning between the m_0 and $m_{1/2}$ parameters as there is in the focus point region. We note that the 1 TeV Higgsino signal can be detected via the associated single-photon process at the 3 TeV CLIC [24,39]. But it is generally believed that there will be no CLIC if there is no SUSY signal at the LHC. In that sense, this region seems to be of little practical interest at least for the colliders.

We shall see below that one obtains a Higgsino LSP dark matter with a mass of 1 TeV in the 75 and 200 models with many properties similar to those of the CMSSM, but with two major advantages. It occurs naturally in these nonuniversal gaugino mass models, without requiring any large cancellation between independent SUSY parameters. Moreover, the corresponding gluino and top-squark masses lie over the 2–3 TeV region, at least a part of which are within the reach of 14 TeV LHC.

IV. PHENOMENOLOGY OF HIGGSINO DARK MATTER IN THE 75 MODEL

Figure 2 shows the $m_{1/2} - m_0$ parameter plane of the NUGM model corresponding to the representation 75 of SU(5) GUT for representative values of $\tan\beta = 10$ and 30 when $A_0 = -3$ TeV. Region I at the top is excluded due to

[3]The limits correspond to a 5σ range of the Planck data that accommodates the WMAP provided range.

[4]We will ignore here the so-called bulk-annihilation region characterized by LSP pair annihilation via t-channel slepton exchange since it occurs for a smaller $m_{1/2}$ zone that is excluded by the Higgs mass data.

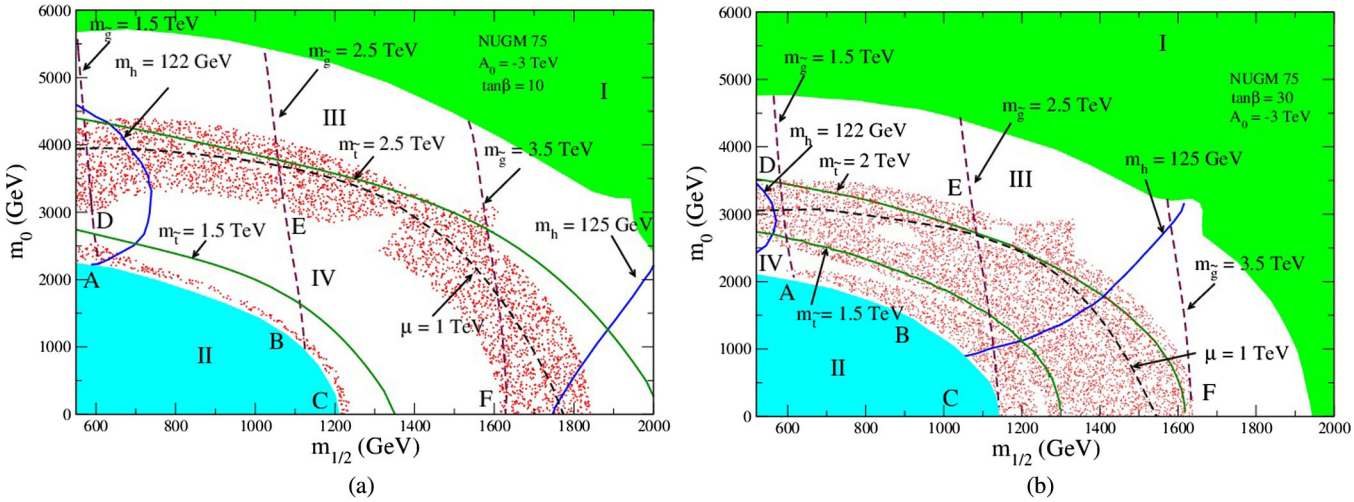

FIG. 2 (color online). (a) Plot in the $m_0 - m_{1/2}$ plane for the 75 model for $\tan\beta = 10$. Region I is excluded because of a nonconvergent EWSB solution. Region II is disfavored, as the top squark becomes the LSP or tachyonic there. Contours for top-squark, gluino masses, $\mu = 1$ TeV, $m_h = 125$ GeV, and $m_h = 122$ GeV are also shown. Red points satisfy the relic density constraint (8). For the red points lying along the boundary of region II in the strip ABC, the LSP is Higgsino like. Along the strip DEF we also find the LSP to be Higgsino like. In the region ABC the main DM annihilating mechanisms are coannihilations involving $\tilde{t}_1, \tilde{\chi}_1^{\pm}, \tilde{\chi}_1^0$, and $\tilde{\chi}_2^0$. All the way along the strip DEF coannihilations occur where $\tilde{\chi}_1^{\pm}$, $\tilde{\chi}_1^0$, and $\tilde{\chi}_2^0$ take part almost equally. In regions III and IV we obtain underabundant and overabundant DM, respectively. The entire parameter space is allowed by $B_s \to \mu^+\mu^-$ and $b \to s\gamma$ constraints. (b) Similar plot as in panel (a) with $\tan\beta = 30$. Colors and conventions are the same as in panel (a). Here we get underabundant DM for both regions III and IV.

the nonconvergent EWSB solution, while region II at the bottom is excluded due to the lighter top squark ($\tilde{t}_1$) being the LSP/tachyonic for both Fig. 2(a) and Fig. 2(b). The regions with red dots correspond to Higgsino dark matter that satisfy the cosmological relic density, while the constraints from the Higgs boson mass range of 122–125 GeV are indicated by the blue solid lines. Contours of gluino and lighter top-squark masses are indicated along with the $\mu = 1$ TeV contour. In the band DEF the cosmological relic density of dark matter is achieved through coannihilation among the degenerate charged and neutral Higgsinos ($\tilde{\chi}_1^0, \tilde{\chi}_2^0, \tilde{\chi}_1^{\pm}$), while in the strip ABC near the lower boundary there is additional coannihilation with the lighter top squark ($\tilde{t}_1$). In regions III and IV we obtain underabundant and overabundant DM, respectively, for Fig. 2(a), whereas the regions labeled III and IV correspond to only underabundant DM in Fig. 2(b). $B_s \to \mu^+\mu^-$ and $b \to s\gamma$ constraints are satisfied everywhere. We now comment on the appearance of the *clip* regions in both of the above figures. We have investigated it by varying m_0 for a given $m_{1/2}$ in relevant regions. A jump in μ appears near a particular zone of m_0 associated with the *clip* region. This is essentially associated with the way the corrections to μ^2 arising out of a finite-order effective potential (one or two loop) are computed [40]. It is possible that a logarithmic term for the correction (typically from the top-squark contribution) may turn from a negative value to a positive value almost discontinuously for a small change in m_0 around a given value of m_0. This would give rise to a jump in the value of μ. For a Higgsino-dominated LSP, such an abrupt (albeit small change) in μ may mean a significant amount of change in the relic density ($\sim\mu^2$). Thus the above explains the appearance of *clip* regions within the zone that satisfies the relic density. A similar effect occurs in the zone near the REWSB boundary. Of course, the inclusion of higher-order terms in the effective potential would smooth out such jumps or eliminate the *clip* regions in general.

Table II lists the superparticle masses for three benchmark points (BP) from the left part of each figure [namely, Figs. 2(a) and 2(b)] with relatively light gluinos, which can be probed at the high-luminosity run of the 14 TeV LHC. Here we show the gluino pair-production cross section for these points at the 14 TeV LHC as obtained by using the code PROSPINO [41]. These cross sections correspond to several hundred gluino pairs at 100 fb^{-1} which can be probed in the high-luminosity run of LHC. Moreover, the probe can be extended up to a gluino mass of 2.5 TeV at the very high-luminosity runs of 1000–3000 fb^{-1} [42]. We note that Table II shows an inverted hierarchy of squark masses with a relatively light top squark $\tilde{t}_1$. Together with the large coupling of the top squark with the Higgsino, it implies that the gluino will dominantly decay via a real or virtual top squark: $\tilde{g} \to t\bar{t}\tilde{\chi}_{1,2}^0$. In the second to last row we show the branching ratio (BR) results from SUSY-HIT [43] for the dominant decay modes of $\tilde{g}$. Only the modes having BR $> 10\%$ are shown. For BPs 1, 3, 4, and 6, $\tilde{g}$ decays to $\tilde{t}_1\bar{t}$-type final states with 100% BR. As shown in the last row, $\tilde{t}_1$ further decays to $b\tilde{\chi}_1^+$ since kinematically there is no

TABLE II. Spectra of six benchmark points for the 75 model. Masses and mass parameters are shown in GeV. Gluino pair-production cross sections correspond to a 14 TeV LHC run. The relevant SM parameters used are $m_t^{\rm pole} = 173.5$ GeV, $m_b^{\overline{\rm MS}} = 4.18$ GeV, and $m_\tau = 1.77$ GeV. Branching ratios for the dominant decay modes of $\tilde{g}$ and $\tilde{t}_1$ are also shown.

Parameter	1	2	3	4	5	6
$m_{1/2}$	837.11	731.80	658.32	843.10	762.16	656.10
m_0	1948.54	3689.09	2248.34	1805.52	3110.81	2089.04
$\tan\beta$	10.00	10.00	10.00	30.00	30.00	30.00
A_0	−3000.00	−3000.00	−3000.00	−3000.00	−3000.00	−3000.00
(M_1,M_2,M_3)	1884, 2035. 1767	1661, 1786, 1517	1475,1599,1400	1895,2052,1786	1724, 1860, 1593	1467,1595, 1403
μ	1268.56	1062.37	1235.64	1176.45	978.18	1148.12
$m_{\tilde{g}}$	1954.41	1822.47	1600.97	1957.89	1861.66	1587.32
$m_{\tilde{\chi}_1^\pm}, m_{\tilde{\chi}_2^\pm}$	1272.51, 2081.25	1072.96, 1854.31	1234.37, 1650.76	11 81.44, 2095.35	988.12, 1922.20	1148.78, 1643.44
$m_{\tilde{\chi}_1^0}, m_{\tilde{\chi}_2^0}$	1272.18, 1275.75	1072.59, 1076.29	1233.99, 1240.02	1180.92, 1183.69	987.55, 990.32	1148.18, 1152.51
$m_{\tilde{t}_1}, m_{\tilde{t}_2}$	1298.52, 2421.22	2188.85, 3365.72	1282.69, 2287.72	1270.36, 2235.20	1909.76, 2838.59	1220.38, 2054.05
$m_{\tilde{b}_1}, m_{\tilde{b}_2}$	2412.53, 2486.19	3364.03, 3866.90	2279.98, 2533.74	2098.72, 2229.44	2835.95, 3048.80	2038.31, 2127.47
$m_{\tilde{u}_1}, m_{\tilde{u}_2}$	2922.94, 2671.38	4104.89, 3982.31	2818.42, 2661.21	2848.60, 2584.39	3657.64, 3500.96	2697.29, 2531.82
$m_{\tilde{e}_L}, m_{\tilde{e}_R}$	2620.75, 2480.56	3978.62, 3919.23	2633.97, 2550.39	2527.42, 2377.81	3485.48, 3405.96	2499.53, 2410.04
$m_{\tilde{\tau}_1}, m_{\tilde{\tau}_2}$	2450.19, 2606.89	3881.97, 3960.64	2519.42, 2619.58	2096.37, 2402.7 6	3078.22, 3331.77	2122.94, 2368.87
$m_A, m_{H^\pm}$	2873.09, 2873.11	4068.20, 4068.24	2865.53, 2865.33	2210.31, 2210.25	2913.68, 2913.65	2179.37, 2179.33
m_h	123.13	122.04	122.20	123.95	122.87	123.03
$\Omega_{\tilde{\chi}_1} h^2$	0.11	0.13	0.12	0.12	0.11	0.10
$BF(b\to s\gamma)$	3×10^{-4}	3.04×10^{-4}	3×10^{-4}	2.77×10^{-4}	2.91×10^{-4}	2.75×10^{-4}
$BF(B_s\to\mu^+\mu^-)$	3.53×10^{-9}	3.53×10^{-9}	3.53×10^{-9}	3.76×10^{-9}	3.58×10^{-9}	3.76×10^{-9}
$\sigma_{p\chi}^{\rm SI}$ in pb	7×10^{-10}	7.57×10^{-10}	2.97×10^{-9}	4.54×10^{-10}	4.11×10^{-10}	1.74×10^{-9}
$\sigma_{gg}^{\rm NLO}$ in fb	1.23	2.83	8.45	1.19	2.21	8.97
Dominant decay modes of $\tilde{g}$ (in %) (> 10% are shown)	$\tilde{g}\to\tilde{t}_1\bar{t}$ 50 $\to\tilde{t}_1^* t$ 50	$\tilde{g}\to\tilde{\chi}_1^0 t\bar{t}$ 23 $\to\tilde{\chi}_2^0 t\bar{t}$ 18 $\to\tilde{\chi}_1^- t\bar{b}$ 27 $\to\tilde{\chi}_1^+ b\bar{t}$ 27	$\tilde{g}\to\tilde{t}_1\bar{t}$ 50 $\to\tilde{t}_1^* t$ 50	$\tilde{g}\to\tilde{t}_1\bar{t}$ 50 $\to\tilde{t}_1^* t$ 50	$\tilde{g}\to\tilde{\chi}_1^0 t\bar{t}$ 23 $\to\tilde{\chi}_2^0 t\bar{t}$ 20 $\to\tilde{\chi}_1^- t\bar{b}$ 27 $\to\tilde{\chi}_1^+ b\bar{t}$ 27	$\tilde{g}\to\tilde{t}_1\bar{t}$ 50 $\to\tilde{t}_1^* t$ 50
Dominant decay modes of $\tilde{t}_1$ (in %) (> 10% are shown)	$\tilde{t}_1\to b\tilde{\chi}_1^+$ 100	⋯	$\tilde{t}_1\to b\tilde{\chi}_1^+$ 100	$\tilde{t}_1\to b\tilde{\chi}_1^+$ 100	⋯	$\tilde{t}_1\to b\tilde{\chi}_1^+$ 100

way to have a top and an LSP for the above decay. On the other hand, for BPs 2 and 5, the $\tilde{g}\to\tilde{t}_1\bar{t}$ decay mode is kinematically forbidden, leading to $\tilde{g}$ decaying into three-body final states. It is clear from the BRs that the signal will contain two to four top quarks plus a large E_T from the decay of the gluino pair. Moreover, the Majorana nature of the gluino implies that half of the two top quarks plus E_T final states will have a same-sign top-quark pair. Thus, one expects a distinctive signal with either two same-sign top quarks or three or four top quarks accompanied by a large E_T from the LSP pair. Depending on the BPs or the parameter space, in general one needs to carefully compute the SM backgrounds [44]. We hope the members of the ATLAS and CMS collaborations will make detailed simulation studies of this signal, which is beyond the scope of the present work. We shall proceed now to the model predictions for the direct and indirect dark matter detection experiments.

The spin-independent scattering cross section $\sigma_{p\tilde{\chi}_1^0}^{\rm SI}$ of the nucleon with $\tilde{\chi}_1^0$ involves Higgs exchange (t-channel) or squark exchange (s-channel) diagrams. With the present LHC limit of squark masses, the Higgs exchange processes dominate in $\sigma_{p\tilde{\chi}_1^0}^{\rm SI}$. Typically, unless the LSP is a mixture of Higgsino with bino or wino, the couplings are suppressed. For a Higgsino-dominated scenario of the LSP with $\tilde{\chi}_1^0$ ($|\mu| \ll M_1, M_2$) and for the decoupling limit of the Higgs boson ($M_Z^2 \ll M_A^2$), one finds the relevant couplings [45] $C_{h\tilde{\chi}\tilde{\chi}}$ and $C_{H\tilde{\chi}\tilde{\chi}}$ that explicitly show the suppression effect when M_1 and M_2 are away from μ. The results are not however valid when $|\mu|$ is close to either M_1 or M_2:

$$C_{h\tilde{\chi}\tilde{\chi}} \simeq \mp\frac{1}{2} M_Z c_W [1 \pm \sin 2\beta]\left[\frac{t_W^2}{M_1 - |\mu|} + \frac{1}{M_2 - |\mu|}\right],$$
$$C_{H\tilde{\chi}\tilde{\chi}} \simeq \frac{1}{2} M_Z c_W \cos 2\beta\left[\frac{t_W^2}{M_1 - |\mu|} + \frac{1}{M_2 - |\mu|}\right], \qquad (10)$$

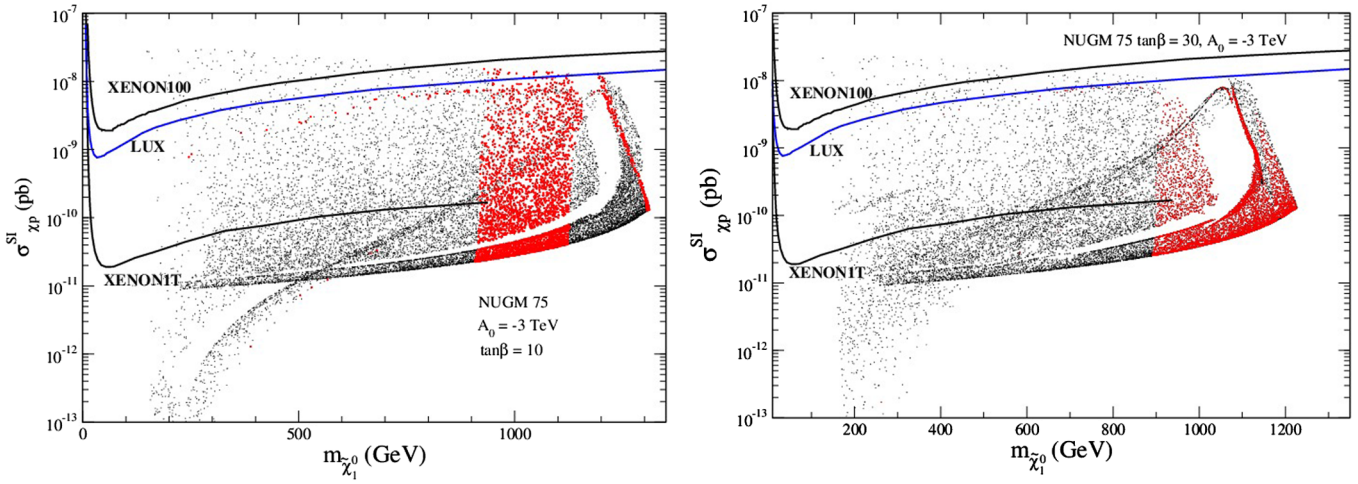

FIG. 3 (color online). (a) Spin-independent scattering cross section of the LSP with a proton as a function of LSP mass for the 75 model with $\tan\beta = 10$. The constraints coming from direct-detection experiments—like XENON100, LUX, and the expected limit from XENON1T—are shown. The points in red satisfy the relic density constraint. (b) Similar plot as in panel (a) for $\tan\beta = 30$.

for $\mu > 0$ and $\mu < 0$, respectively, with $s_W = \sin\theta_W$, etc. The particular result to note from the above equation for the Higgsino-dominated LSP case is that the direct-detection SI cross section decreases with an increase in the gaugino masses M_1 and M_2. Thus for a given $m_{1/2}$, the 75 model will have a decreased value for $\sigma^{\rm SI}_{p\tilde{\chi}^0_1}$ because of larger values of the bino and wino masses when compared with the mSUGRA scenario. Figures 3(a) and 3(b) show the results of $\sigma^{\rm SI}_{p\tilde{\chi}^0_1}$ for different values of the LSP mass for $\tan\beta = 10$ and $\tan\beta = 30$ using micrOMEGAs [46]. This corresponds to the parameter space of Fig. 2. The exclusion contours from XENON100 [47] and LUX [48] are also shown in addition to the estimated exclusion level for future XENON1T experiment [49]. The regions satisfying the relic density bracketed within $900 < m_{\tilde{\chi}^0_1} < 1300$ GeV for $\tan\beta = 10$ and $900 < m_{\tilde{\chi}^0_1} < 1200$ GeV for $\tan\beta = 30$ are shown in red, and the points generally satisfy the LUX limit. On the other hand, a large region of parameter space may be probed via the future XENON1T experiment.

Coming to the spin-dependent (SD) LSP-proton cross section, we note that $\sigma^{\rm SD}_{p\chi}$ is associated with a Z exchange since the large values of the squark masses after the LHC data would not cause any significant contribution from squark exchange diagrams. The coupling of $\tilde{\chi}^0_1\tilde{\chi}^0_1 Z$ related to a Higgsino asymmetry is given by $C_{Z\tilde{\chi}\tilde{\chi}} = |N^2_{13} - N^2_{14}|$. For a Higgsino-like LSP one can have the following approximate expression [45,50]:

$$C_{Z\tilde{\chi}\tilde{\chi}} \simeq \mp\frac{1}{2}\left[t^2_W\frac{M^2_W}{M_1\mu} + \frac{M^2_W}{M_2\mu}\right]\cos 2\beta + \mathcal{O}\left(\frac{\mu}{M_1}, \frac{\mu}{M_2}\right), \tag{11}$$

for $\mu > 0$ and $\mu < 0$, respectively. We note that for the region of parameter space satisfying the relic density, a Higgsino-dominated LSP when associated with sufficiently large electroweak gaugino masses (which is indeed true for both NUGM models considered in this work) results in a significant amount of suppression of $\sigma^{\rm SD}_{p\chi}$. This is visible in Fig. 4(a) as well as in Fig. 4(b), where we show the scatter plots of $\sigma^{\rm SD}_{p\chi}$ vs $m_{\tilde{\chi}^0_1}$ for $\tan\beta = 10$ and 30, respectively, for the 75 model. For the zones of $m_{\tilde{\chi}^0_1}$ satsfying the relic density, $\sigma^{\rm SD}_{p\chi}$ (shown with red dots) is way too small to be probed via the shown IceCube exclusion limits (both the existing and the projected limits). Here, the spin-dependent cross section is obtained via indirect means by searching for muon neutrinos at IceCube [51] arising out of dark matter annihilation within the Sun. We will also discuss the muon flux limit in relation to the mass of dark matter in this section. We may mention that in the present scenario, the IceCube limits are stronger [52,53] than the dedicated spin-dependent direct-detection experiments like COUPP [54].

We next consider DM indirect-detection studies for the 75 model for the photon signal. There can be a sufficient degree of gravitational capture of weakly interacting massive particles (WIMPs) due to nuclear scattering effects. Gravitational capture may occur in dense regions, like galactic centers, dwarf galaxies or in the core regions of objects within the Solar System such as the Sun or the Earth [4,5]. The LSP pair annihilation would produce fermion-antifermion pairs or electroweak gauge bosons. Decays of products of primary annihilation and hadronization may produce π^0's that would eventually produce photons. Apart from the above there can be final-state radiation effects of primarily produced particles. We note that the environment of gravitational capture and LSP annihilation is associated

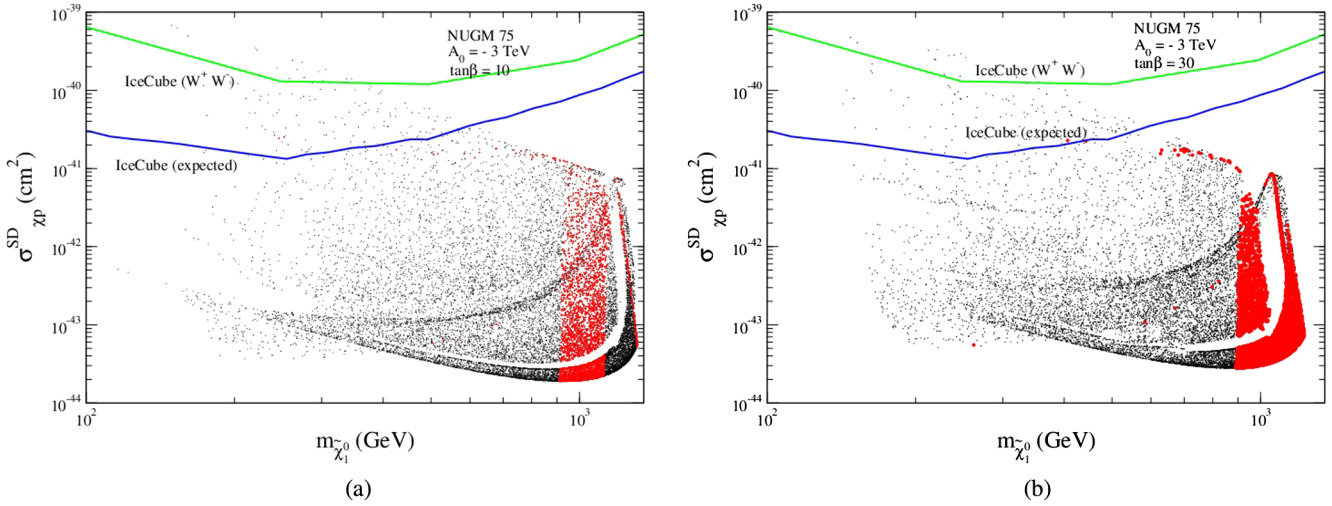

FIG. 4 (color online). (a) Variation of the spin-dependent cross section with the LSP mass for the 75 model with $\tan\beta = 10$. The IceCube exclusion limit for the $\tilde{\chi}_1^0\tilde{\chi}_1^0 \to W^+W^-$ channel is shown as a green line [52]. The blue line represents the expected sensitivity reach of IceCube. (b) Similar plot as in panel (a) for $\tan\beta = 30$.

with a much smaller velocity ($v/c \sim 10^{-3}$), unlike a much larger velocity existing at the time of freeze-out. Thus, the annihilation of LSPs in the present day scenario involves a large p-wave suppression [$(v/c)^2$]. We remind ourselves that the LSP being a Majorana particle the combined CP property and the combined parity of the LSP pair are the same. This makes the favored s-channel particle (namely, the CP-odd Higgs boson A) contribute dominantly to the photon signal, which on the other hand is p-wave suppressed, as discussed above. We note that a larger Higgsino content is generally favorable for the photon signal. However, the NUGM models under discussion depend on high scale input parameters and involve RGEs and REWSB that lead to correlated SUSY spectra. All these cause an s-channel Higgs resonance to become a remote possibility. Figures 5(a) and 5(b) show $\langle\sigma v\rangle$, the thermally averaged LSP pair annihilation cross section, as a function of $m_{\tilde{\chi}_1^0}$ for the 75 model with $\tan\beta = 10$ and $\tan\beta = 30$, respectively. The Fermi-LAT constraint from LAT dwarf spheroidal stacking (4 years) [55] is shown as a green line. The red points correspond to parameter points satisfying the relic density. Owing to a larger $b\bar{b}$ coupling of the Higgs for a large $\tan\beta$, $\langle\sigma v\rangle$ is generally larger in Fig. 5(b) in comparison with Fig. 5(a). The parameter space for the 75 model is practically unconstrained by the present Fermi limit.

We would like to discuss the probing of Higgsino-dominated dark matter via indirect detection of muon flux at IceCube [51] due to neutrinos from the Sun. In SUSY models neutrinos cannot be produced at tree level in

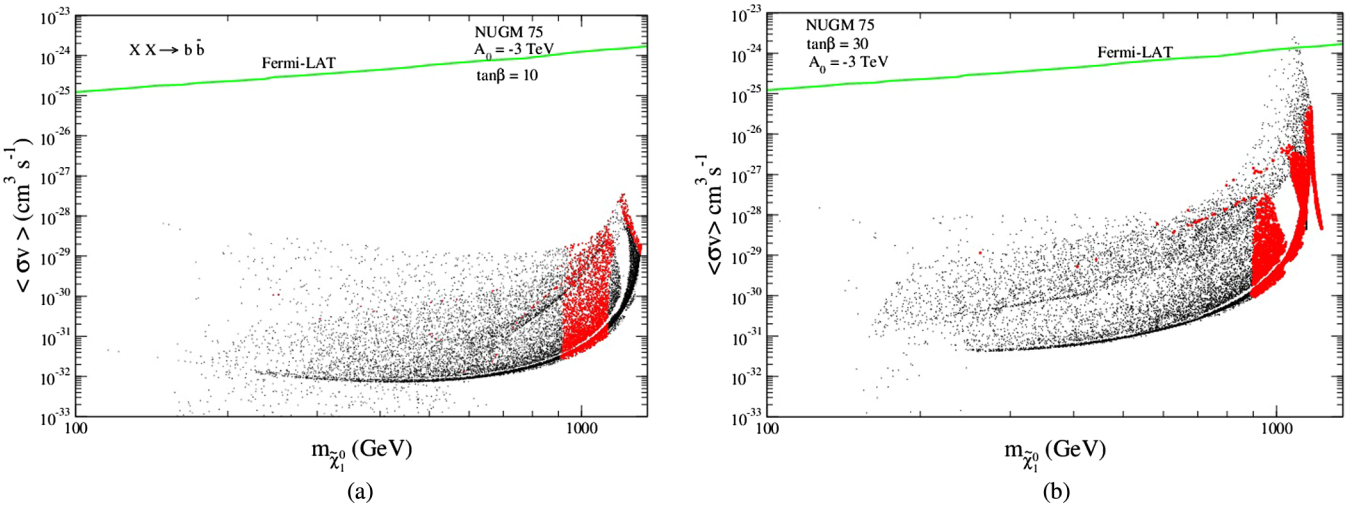

FIG. 5 (color online). (a) DM self-annihilation cross section as a function of DM mass for the 75 model with $\tan\beta = 10$. The Fermi-LAT constraint [LAT dwarf spheroidal stacking (4 years)] [55] is shown as a green line. The parameter space is practically unconstrained by Fermi data. (b) Similar plot as in panel (a) for $\tan\beta = 30$.

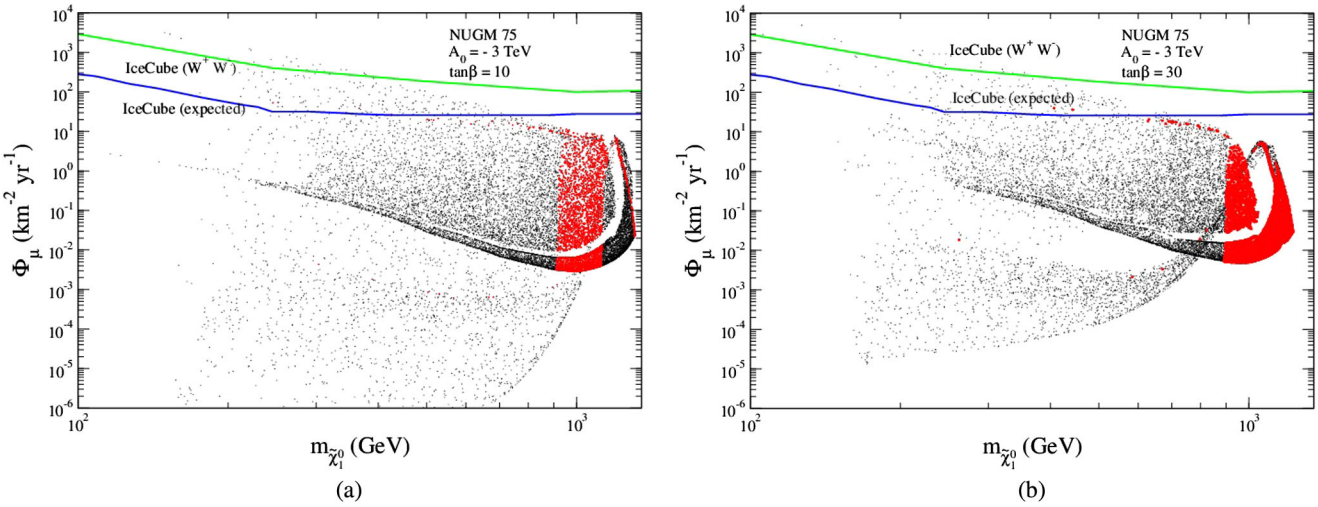

FIG. 6 (color online). (a) Variation of the muon flux with the LSP mass for the 75 model with $\tan\beta = 10$. The IceCube exclusion limit for the $\tilde{\chi}_1^0\tilde{\chi}_1^0 \to W^+W^-$ channel is shown as a green line [52]. The blue line represents the expected sensitivity of IceCube. (b) Similar plot as in panel (a) for $\tan\beta = 30$.

neutralino annihilations. However, neutrinos may arise from other sources, like heavy quarks, gauge bosons, tau leptons, etc.[5] Thus neutrinos are produced with a broad energy distribution, with energy reaching up to a sizable fraction of the DM mass. For a DM mass less than M_W, neutrinos from $b\bar{b}$ or $\tau^+\tau^-$ are the primary channels. But these are not very promising candidates for detection with given experimental thresholds of neutrino detection. For massive neutralinos, annihilations may additionally lead to gauge bosons, top quarks, or Higgs bosons. A neutralino with a substantial Higgsino component may undergo pair annihilation to produce gauge bosons, which in turn may produce high-energy neutrinos. We must keep in mind that neutrinos with an of energy several hundreds of GeV produced inside the Sun would be depleted since the probability of a neutrino escaping the Sun without interaction is given by $P = e^{-E_\nu/E_k}$, where depending on the type of neutrino E_k varies from 130 to 230 GeV [5]. Neutrino oscillation is taken into account while computing the flux of muon neutrinos at the detector. At the detector, the muon flux arising from neutrinos via charge-current interactions is detected.

Neutrino signals from the Sun or other dense regions in general involve the capture and annihilation of WIMPs. In general, both spin-independent and spin-dependent types of scattering of WIMPs with various nuclei may lead to an appreciable reduction of energy, leading to the WIMP velocity going below the escape velocity. This leads to WIMPs being captured within the object and also undergoing pair annihilations. Thus the time evolution of N WIMPs is

$$\frac{dN}{dt} = C - C_A N^2. \tag{12}$$

[5]There is a possibility of having neutrinos from two-to-two annihilation into gauge bosons via loops [56].

Here C refers to the rate at which WIMPs are captured, and C_A depends on the annihilation cross section of WIMPs and is related to the WIMP annihilation rate Γ_A via $\Gamma_A = \frac{1}{2}C_A N^2$ in the Sun [5,57,58]. Any possibility of having a positive evaporation term that is linear in N is neglected here. The above arises from a scenario of WIMP-nuclear scattering, where the WIMP is much lighter than a given nucleus in abundance in the Sun. Such terms may potentially increase the speed of WIMPs above the escape velocity [59]. The time dependence of N from Eq. (12) leads to $\Gamma_A \equiv \frac{1}{2}C_A N^2 = \frac{1}{2}C\tanh^2(t/\tau)$, where $\tau = 1/\sqrt{CC_A}$. With appreciably large capture and annihilation rates, this is indeed possible for the Sun for various models including supersymmetry, and with the present time $t = t^\odot = 4.5 \times 10^9$ years it is realistic to assume $t/\tau \gg 1$, leading to $\Gamma_A = \frac{1}{2}C$. This of course means an equilibrium scenario out of the capture and annihilation of WIMPs [60]. This is however not true for the capture and annihilation of WIMPs in the Earth, which is much less massive, leading to either a much smaller escape velocity or the dominance of spin-independent interactions in the WIMP-nuclear scattering, resulting in reduced capture rates for WIMPs. Thus probing DM via muon flux due to neutrino propagation is not so promising for the Earth when compared to the prospect for the Sun [5]. We must note that both SI and SD cross sections are important for the capture of WIMPs in the Sun [56,61]. Capture cross sections may be related through suitable models to SI and SD WIMP-nuclear cross sections, and it is through such relations that the measurement of muon flux due to neutrino signals may be translated into setting limits on SI and SD cross sections [5,56]. Figures 6(a) and 6(b) show the results of the muon flux with respect to the mass of the LSP for $\tan\beta = 10$ and 30, respectively, for the 75 model. The IceCube exclusion limit for the $\tilde{\chi}_1^0\tilde{\chi}_1^0 \to W^+W^-$ channel is shown as a green line [52].

The blue line represents the expected sensitivity reach of IceCube. Clearly, IceCube would not be able to probe the region of parameter space that satisfies the relic density limits.

V. PHENOMENOLOGY OF HIGGSINO DARK MATTER IN THE 200 MODEL

Figures 7(a) and 7(b) show the scatter plots in the $m_{\frac{1}{2}} - m_0$ plane of the NUGM model corresponding to the representation 200 of SU(5) GUT for representative values of $\tan\beta = 10$ and 30 when $A_0 = -2$ TeV. Region I is excluded because of a nonconvergent EWSB solution. Region II is disallowed because the lighter top squark ($\tilde{t}_1$) becomes the LSP or tachyonic. Contours for squark and gluino masses for a few different values, along with the contours for $\mu = 1$ TeV, $m_h = 122$ GeV, and $m_h = 125$ GeV are also shown. Red points satisfy the relic density constraint. In the region A the LSP is Higgsino-like with very little wino admixture. The mechanisms that allow the DM to satisfy the relic density constraint are coannihilation processes among $\tilde{\chi}_1^{\pm}$, $\tilde{\chi}_1^0$, and $\tilde{\chi}_2^0$. Along the branches B and C the LSP is also Higgsino like. There are coannihilations involving $\tilde{\chi}_1^{\pm}$, $\tilde{\chi}_1^0$, and $\tilde{\chi}_2^0$. Here, we also find $m_{\tilde{\chi}_1^0} \simeq m_{\tilde{\chi}_1^{\pm}} \simeq M_A/2$. Thus we find s-channel Higgs $(A, H, H^{\pm})$ resonance processes involving coannihilations among $\tilde{\chi}_1^0$ and/or $\tilde{\chi}_1^{\pm}/\tilde{\chi}_2^0$. Along the strips DE and EF we also get mostly a Higgsino-like LSP. Here coannihilation processes involving $\tilde{\chi}_1^{\pm}$, $\tilde{\chi}_2^0$, and $\tilde{\chi}_1^0$ cause the dark matter to achieve the right relic density. For regions III, IV, and V we get underabundant DM, whereas regions VI and VII give overabundant DM. The entire parameter space respects $B_s \to \mu^+\mu^-$ and $b \to s\gamma$ constraints.

Table III shows the superpartner masses and other data of phenomenological interest for three benchmark points each for $\tan\beta = 10$ and 30, corresponding to Figs. 7(a) and 7(b), respectively. The mass patterns are more or less not very different from the 75 model. However, we must keep in mind that M_1^G is significantly larger (by a factor of 2), whereas M_2^G is smaller (by a factor of $\frac{2}{3}$) for the 200 model when compared with the 75 model (see Table I). Consequently, the masses of left and right components of scalars are affected differently via RGE effects. The change happens such that almost all the squarks and the sleptons are split among the left and right scalars in the 200 model. The top-squark sector has a reduced splitting because of the smaller $|A_0|$ considered here compared to the 75 model. The second to last row shows the gluino pair-production cross section [at next-to-leading order (NLO)] at the 14 TeV LHC using PROSPINO [41]. Typically these would correspond to fewer gluino pairs compared to the 75 model. Nonetheless, they correspond to around 100 events in the high-luminosity 100 fb^{-1} run of LHC. The decay modes of $\tilde{g}$ are more or less the same as those of the 75

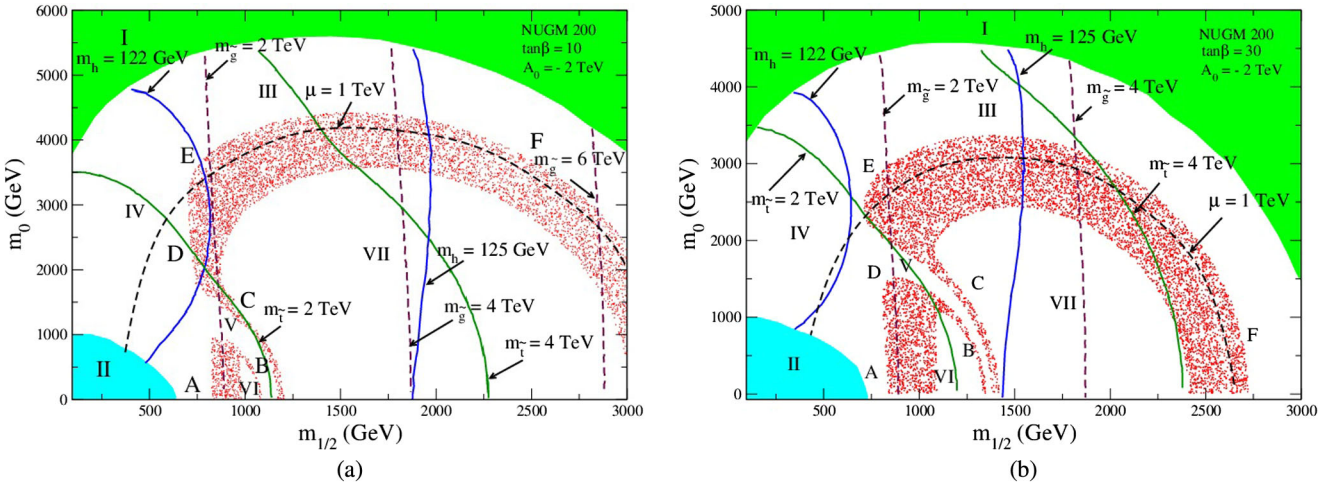

FIG. 7 (color online). (a) Allowed parameter space in the $m_0 - m_{1/2}$ plane for the 200 model for $\tan\beta = 10$. Region I is excluded because of a nonconvergent EWSB solution. Region II is disallowed because the top squark becomes the LSP or tachyonic. Contours for the squark and gluino masses, $\mu = 1$ TeV, $m_h = 122$ GeV, and $m_h = 125$ GeV are also shown. Red points satisfy the relic density constraint. In region A the LSP is Higgsino like with very little wino admixture. The mechanisms that allow the DM to satisfy the WMAP relic density constraint are coannihilation processes among $\tilde{\chi}_1^{\pm}$, $\tilde{\chi}_1^0$, and $\tilde{\chi}_2^0$. Along the branches B and C the LSP is Higgsino like. There are coannihilations involving $\tilde{\chi}_1^{\pm}$, $\tilde{\chi}_1^0$, and $\tilde{\chi}_2^0$. Here we also find $m_{\tilde{\chi}_1^0} \simeq m_{\tilde{\chi}_1^{\pm}} \simeq M_A/2$. Thus we find s-channel Higgs $(A, H, H^{\pm})$ resonance processes involving coannihilations among $\tilde{\chi}_1^0$ and/or $\tilde{\chi}_1^{\pm}/\tilde{\chi}_2^0$. Along the strips DE and EF we also get mostly a Higgsino-like LSP, and coannihilation among $\tilde{\chi}_1^{\pm}$, $\tilde{\chi}_2^0$, and $\tilde{\chi}_1^0$ helps the dark matter to achieve the right relic density. For regions III, IV, and V we get underabundant DM, whereas regions VI and VII give overabundant DM. The parameter space is unconstrained by $B_s \to \mu^+\mu^-$ and $b \to s\gamma$ limits. (b) Similar plot as in panel (a) for $\tan\beta = 30$.

TABLE III. Spectra of six benchmark points for the 200 model. Masses and mass parameters are shown in GeV. Gluino pair-production cross sections correspond to a 14 TeV LHC run. Branching ratios for the dominant decay modes of $\tilde{g}$, $\tilde{t}_1$, and $\tilde{b}_1$ are also shown.

Parameter	1	2	3	4	5	6
$m_{1/2}$	848.94	818.46	874.26	833.33	732.93	881.86
m_0	1663.05	2847.18	895.64	1102.62	2587.57	644.69
$\tan\beta$	10.00	10.00	10.00	30.00	30.00	30.00
A_0	−2000.00	−2000.00	−2000.00	−2000.00	−2000.00	−2000.00
(M_1, M_2, M_3)	3781, 1364, 1779	3670, 1318, 1695	3880, 1402, 1842	3696, 1338, 1763	3272, 1181, 1534	3912, 1416, 1865
μ	1224.92	1096.58	1278.14	1180.55	962.14	1224.61
$m_{\tilde{g}}$	1976.53	1969.82	1989.92	1911.12	1779.53	1993.02
$m_{\tilde{\chi}_1^\pm}, m_{\tilde{\chi}_2^\pm}$	1215.42, 1420.40	1096.80, 1380.77	1264.42, 1453.96	11 71.41, 1386.67	961.65, 1238.37	1216.89, 1459.56
$m_{\tilde{\chi}_1^0}, m_{\tilde{\chi}_2^0}$	1214.18, 1235.18	1095.45, 1110.36	1263.25, 1286.26	1170.02, 1187.81	960.01, 974.02	1215.54, 1231.19
$m_{\tilde{t}_1}, m_{\tilde{t}_2}$	1935.09, 2143.44	2413.91, 2711.43	1660.69, 2004.42	1577.30, 1957.53	2151.43, 2334.72	1512.69, 1995.50
$m_{\tilde{b}_1}, m_{\tilde{b}_2}$	2002.13, 2467.81	2696.88, 3302.78	1699.20, 2111.78	1605.97, 1946.00	2298.94, 2754.09	1533.65, 1863.84
$m_{\tilde{u}_1}, m_{\tilde{u}_2}$	2545.05, 3064.03	3362.44, 3751.19	2203.44, 2812.92	2213.15, 2771.82	3049.81, 3394.37	2137.80, 2770.35
$m_{\tilde{e}_L}, m_{\tilde{e}_R}$	2510.23, 3534.60	3364.87, 4134.98	2140.52, 3338.13	2156.49, 3258.35	3047.09, 3731.57	2066.61, 3308.62
$m_{\tilde{\tau}_1}, m_{\tilde{\tau}_2}$	2493.40, 3510.79	3346.80, 4105.56	2123.61, 3316.60	2001.68, 3055.4 0	2888.06, 3469.38	1907.25, 3112.53
$m_A, m_{H^\pm}$	2757.87, 2757.70	3498.83, 3498.88	2462.24, 2462.44	2011.60, 2011.60	2612.90, 2612.90	1966.87, 1966.85
m_h	122.42	122.01	122.90	123.42	122.45	123.77
$\Omega_{\tilde{\chi}_1} h^2$	0.11	0.12	0.10	0.10	0.09	0.10
$BF(b \to s\gamma)$	3.02×10^{-4}	3.04×10^{-4}	3.01×10^{-4}	2.78×10^{-4}	2.88×10^{-4}	2.78×10^{-4}
$BF(B_s \to \mu^+\mu^-)$	3.53×10^{-9}	3.53×10^{-9}	3.54×10^{-9}	3.78×10^{-9}	3.79×10^{-9}	3.81×10^{-9}
$\sigma_{p\chi}^{\rm SI}$ in pb	1.41×10^{-8}	7.46×10^{-9}	1.65×10^{-8}	1.15×10^{-8}	6.54×10^{-9}	9.44×10^{-9}
$\sigma_{gg}^{\rm NLO}$ in fb	1.09	1.26	9.73×10^{-1}	1.47	3.31	9.51×10^{-1}
Dominant decay modes of $\tilde{g}$ in (%) (> 10% are shown)	$\tilde{g} \to \tilde{\chi}_1^0 t\bar{t}$ 12 $\to \tilde{\chi}_2^0 t\bar{t}$ 11 $\to \tilde{\chi}_1^- t\bar{b}$ 22 $\to \tilde{\chi}_1^+ b\bar{t}$ 22 …	$\tilde{g} \to \tilde{\chi}_1^0 t\bar{t}$ 20 $\to \tilde{\chi}_2^0 t\bar{t}$ 17 $\to \tilde{\chi}_1^- t\bar{b}$ 23 $\to \tilde{\chi}_1^+ b\bar{t}$ 23 …	$\tilde{g} \to \tilde{b}_1 \bar{b}$ 29.5 $\to \tilde{b}_1^* b$ 29.5 $\to \tilde{t}_1 \bar{t}$ 20.5 $\to \tilde{t}_1^* t$ 20.5	$\tilde{g} \to \tilde{b}_1 \bar{b}$ 29 $\to \tilde{b}_1^* b$ 29 $\to \tilde{t}_1 \bar{t}$ 21 $\to \tilde{t}_1^* t$ 21	$\tilde{g} \to \tilde{\chi}_1^0 t\bar{t}$ 17 $\to \tilde{\chi}_2^0 t\bar{t}$ 14 $\to \tilde{\chi}_1^- t\bar{b}$ 23 $\to \tilde{\chi}_1^+ b\bar{t}$ 23 …	$\tilde{g} \to \tilde{b}_1 \bar{b}$ 26 $\to \tilde{b}_1^* b$ 26 $\to \tilde{t}_1 \bar{t}$ 22 $\to \tilde{t}_1^* t$ 22
Dominant decay modes of $\tilde{t}_1/\tilde{b}_1$ (in %) (> 10% are shown)			$\tilde{t}_1 \to t\tilde{\chi}_1^0$ 24 $\to t\tilde{\chi}_2^0$ 38 $\to b\tilde{\chi}_1^+$ 27 $\tilde{b}_1 \to t\tilde{\chi}_1^-$ 64 $\to t\tilde{\chi}_2^-$ 23	$\tilde{t}_1 \to t\tilde{\chi}_1^0$ 24 $\to t\tilde{\chi}_2^0$ 36 $\to b\tilde{\chi}_1^+$ 30 $\tilde{b}_1 \to t\tilde{\chi}_1^-$ 61 $\to t\tilde{\chi}_2^-$ 14 $\to b\tilde{\chi}_1^0$ 10		$\tilde{t}_1 \to t\tilde{\chi}_1^0$ 23 $\to t\tilde{\chi}_2^0$ 42 $\to b\tilde{\chi}_1^+$ 33 $\tilde{b}_1 \to t\tilde{\chi}_1^-$ 74 $\to b\tilde{\chi}_1^0$ 14 $\to b\tilde{\chi}_2^0$ 10

model for BPs 1, 2, and 5, leading to similar signal characteristics. For BPs 3, 4, and 6 there is an additional decay mode, $\tilde{g} \to \tilde{b}_1 \bar{b}$, which was absent in the 75 case. The reason lies in the fact that $\tilde{t}_1$ and $\tilde{b}_1$ have similar masses here compared to the 75 case. Furthermore, the last row shows the relevant BRs for the decays of $\tilde{t}_1$ and $\tilde{b}_1$. We note that $\tilde{b}_1$ dominantly decays in the channel $\tilde{b}_1 \to t\tilde{\chi}_1^-$. So, as in the 75 model, the gluino pair will decay dominantly into two, three, or four top quarks plus E_T, with half of the two top events having same-sign tops.

Figures 8(a) and 8(b) show the scatter plots of the spin-independent direct-detection cross section of neutralino dark matter with respect to the mass of the LSP in the 200 model for $\tan\beta = 10$ and 30, respectively. The exclusion contours from XENON100 [47] and LUX [48] are also shown, in addition to the estimated exclusion level for the future XENON1T experiment [49]. The region $900 < m_{\tilde{\chi}_1^0} < 1400$ GeV (which satisfies the relic density) for both values of $\tan\beta$ are shown in red, and an appreciable number of parameter points are discarded via the LUX limit. On the other hand, a large region of parameter space may be probed via the future XENON1T experiment. We note that the 200 model has a smaller wino mass (M_2) compared to that for the 75 model for a given value of $m_{1/2}$. Thus the SI cross section can be understood to be larger for the 200 model [Eq. (10)] due to the relative closeness of values between μ and M_2. Consequently, a larger region of parameter space in the 200 model is excluded via the LUX limit in comparison with the 75 model (Fig. 3).

Figures 9(a) and 9(b) show the scatter plots of $\sigma_{p\chi}^{\rm SD}$ vs $m_{\tilde{\chi}_1^0}$ for $\tan\beta = 10$ and 30, respectively, for the 200 model.

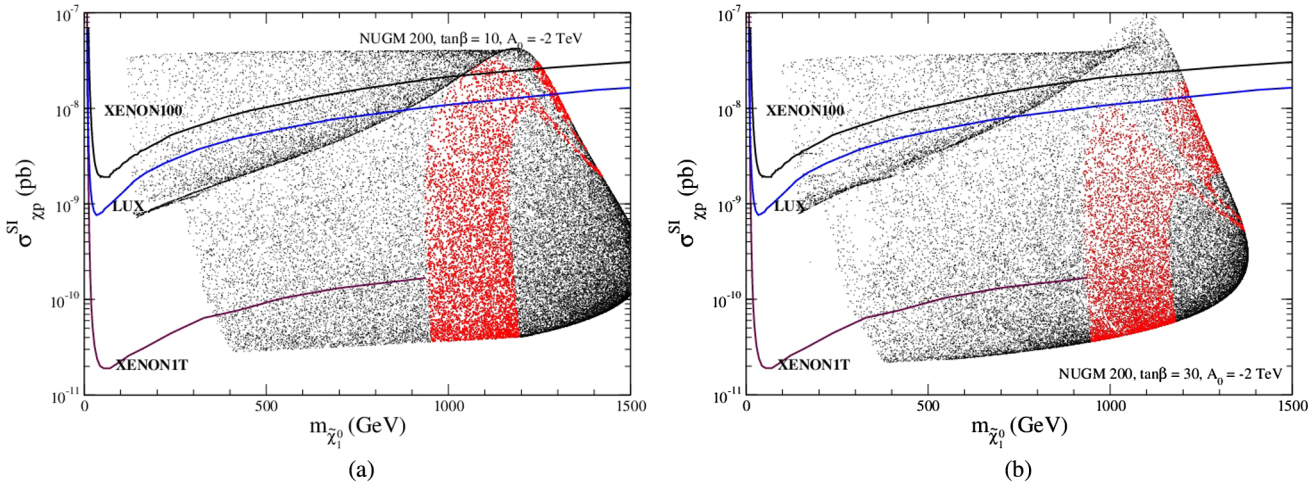

FIG. 8 (color online). (a) Spin-independent scattering cross section of the LSP with a proton as a function of LSP mass for the 200 model with $\tan\beta = 10$. The constraints coming from direct-detection experiments—like XENON100, LUX, and the future XENON1T experiment—are shown. (b) Similar plot as in panel (a) for $\tan\beta = 30$.

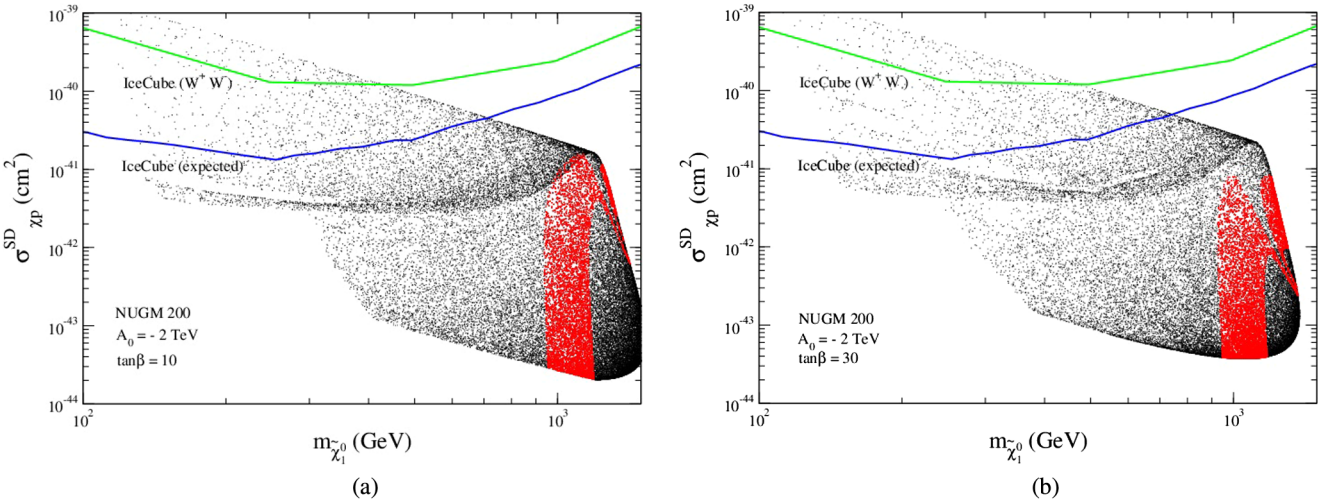

FIG. 9 (color online). (a) Variation of the spin-dependent cross section with the LSP mass for the 200 model with $\tan\beta = 10$. The IceCube exclusion limit for the $\tilde{\chi}_1^0\tilde{\chi}_1^0 \to W^+W^-$ channel is shown as a green line. The blue line represents the expected sensitivity reach of IceCube. (b) Similar plot as in panel (a) for $\tan\beta = 30$.

For the zones of $m_{\tilde{\chi}_1^0}$ satisfying the relic density, $\sigma_{p\chi}^{\mathrm{SD}}$ (as shown with red dots) is way too small to be probed via the shown IceCube exclusion limits (both the existing and projected limits). As mentioned before, here the spin-dependent cross section is obtained via indirect means by searching for muon neutrinos at IceCube [51] arising from dark matter annihilation within the Sun. We note that in comparison with the 75 model (Fig. 4) the SD cross section is a little larger in the 200 model because of the relatively smaller mass of the wino [Eq. (11)]. We will soon discuss the muon flux limit in relation to the mass of dark matter.

Figures 10(a) and 10(b) show $\langle\sigma v\rangle$ as a function of $m_{\tilde{\chi}_1^0}$ for the 200 model with $\tan\beta = 10$ and $\tan\beta = 30$, respectively. The Fermi-LAT constraint [LAT dwarf spheroidal stacking (4 years) [55]] is shown as a green line. The red points correspond to parameter points that satisfy the relic density bound. Similar to Fig. 5, the parameter space for the 200 model is practically unconstrained by the present Fermi limit.

Figures 11(a) and 11(b) show the results of the muon flux with respect to the mass of the LSP for $\tan\beta = 10$ and 30, respectively, for the 200 model. The IceCube exclusion limit for the $\tilde{\chi}_1^0\tilde{\chi}_1^0 \to W^+W^-$ channel is shown as a green line [52]. The blue line represents the expected sensitivity reach of IceCube. Clearly, IceCube would not be able to probe the region of parameter space that satisfies the relic density limits.

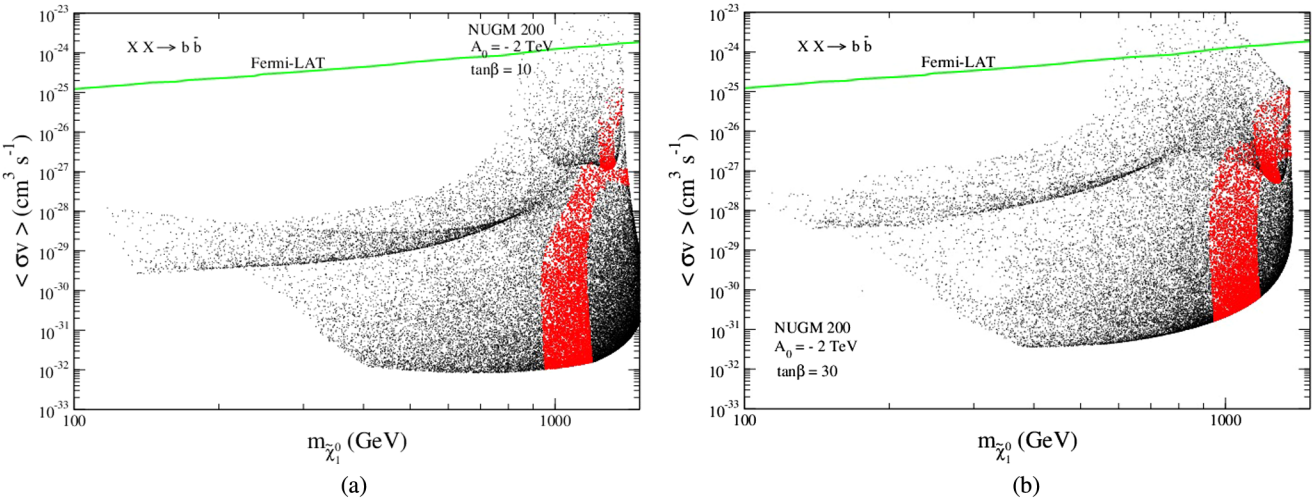

FIG. 10 (color online). (a) DM self-annihilation cross section as a function of DM mass for the 200 model with $\tan\beta = 10$. The Fermi-LAT constraint [LAT dwarf spheroidal stacking (4 years)] [55] is shown as a green line. The parameter space is practically unconstrained by Fermi data. (b) Similar plot as in panel (a) for $\tan\beta = 30$.

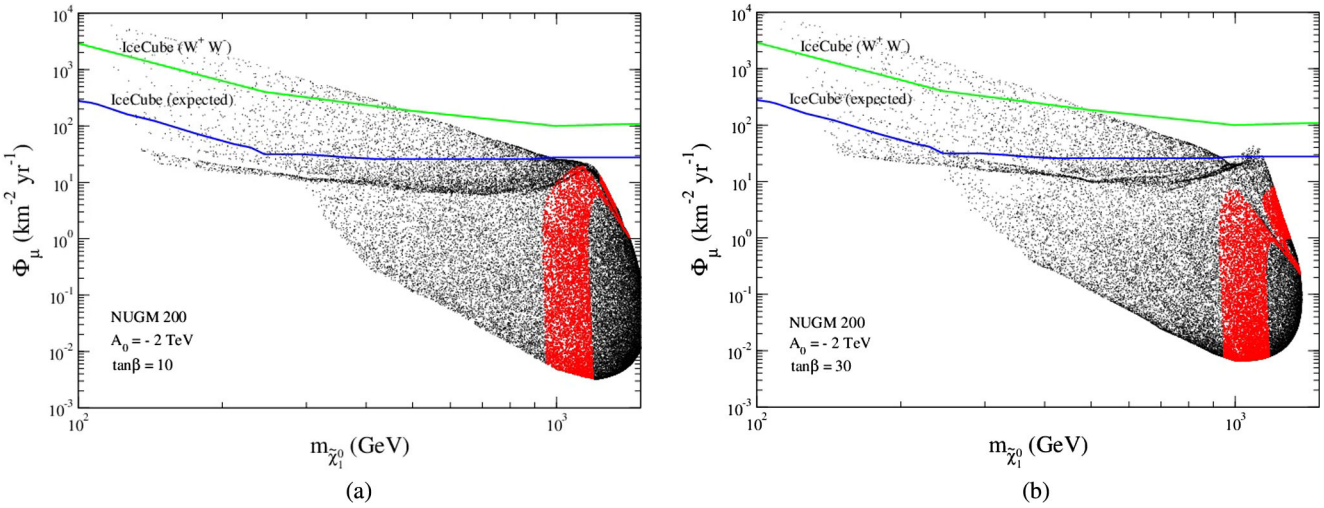

FIG. 11 (color online). (a) Variation of the muon flux with the LSP mass for the 200 model with $\tan\beta = 10$. The IceCube exclusion limit for the $\tilde{\chi}_1^0\tilde{\chi}_1^0 \to W^+W^-$ channel is shown as a green line. The blue line represents the expected sensitivity reach of IceCube. (b) Similar plot as in panel (a) for $\tan\beta = 30$.

VI. CONCLUSION

The LHC SUSY searches and discovery of a Higgs boson at 125 GeV have put strong lower bounds on superparticle masses. Consequently, the CMSSM/mSUGRA with a typically bino-dominated LSP leads to an overabundance of the DM relic density over most of its parameter space. There are only a few strips of parameter space that give a relic density that is compatible with WMAP/Planck data, each of which requires a significant amount of fine-tuning amongst the SUSY mass parameters. Moreover, large parts of the stau coannihilation region and the resonant annihilation region are disallowed by the Higgs mass constraint, while the focus-point region is strongly disfavored by the direct DM search experiments. The Higgsino LSP region can account for the right DM relic density for an LSP mass of about 1 TeV, while satisfying the Higgs mass and other experimental constraints; however, it implies large squark/gluino masses $\gtrsim$8–10 TeV, which are inaccessible at LHC. On the other hand, nonuniversal gaugino mass models corresponding to the 75 and 200 representations of the SU(5) GUT group naturally predict a Higgsino-dominated LSP, which can account for the right DM relic density for an LSP mass of

about 1 TeV (as in the case of the CMSSM) but with much reduced fine-tuning. Moreover, it implies gluino masses in the region of 2–3 TeV in these models, at least a part of which is accessible to high-luminosity LHC runs at 14 TeV. We listed the SUSY spectra for a set of benchmark points in this region of the two nonuniversal guino mass models along with the corresponding gluino pair-production cross sections at 14 TeV LHC. We also briefly discussed the distinctive signatures of these signal events. We then discussed the prospects of detecting these two model signals in various direct and indirect DM detection experiments. For both of the models these signal cross sections turn out to be quite small. The smallness of the spin-independent direct-detection cross section $\sigma^{\rm SI}_{p\chi}$ in the above two models arises from the fact that (i) the LSP is mostly Higgsino like with very little bino or wino components, and (ii) the masses of the bino and wino in the two models are large for a given gluino mass in comparison to what is found in the CMSSM. $\sigma^{\rm SI}_{p\chi}$ is a little higher in the 200 model compared to that in the 75 model because of a relatively smaller wino mass for the former model. The results show that a significant amount of parameter space is allowed by LUX and will be probed by future direct-detection experiments like XENON1T. We also evaluated the spin-dependent cross section $\sigma^{\rm SD}_{p\chi}$ for the two models. It was found that for the characteristic zones of $m_{\tilde{\chi}^0_1}$ that satisfy the relic density limits, the masses of the bino and wino are sufficiently high so as to cause some suppression effect. $\sigma^{\rm SD}_{p\chi}$ becomes quite small, which will be probed via IceCube. Regarding the indirect-detection signals, the photon signal intensity is small because of a general lack of s-channel Higgs resonance arising from the characteristic spectra of NUGM models that involve the given mass relations among gaugino mass parameters, RGEs, and REWSB. The thermally averaged annihilation cross section lies well below the Fermi-LAT limit. Similarly, the muon flux values are too low to be probed by IceCube. One finds that the two NUGM models would be probed better using the measurement of the spin-independent direct-detection cross section via XENON1T rather than any other direct and indirect dark matter detection experiments.

ACKNOWLEDGMENTS

D. P. R. was partly supported by the senior scientist fellowship of Indian National Science Academy. M. C. would like to thank the Council of Scientific and Industrial Research, Government of India for support.

[1] For reviews on supersymmetry, see, e.g., H. P. Nilles, Phys. Rep. **110**, 1 (1984); J. D. Lykken, arXiv:hep-th/9612114; J. Wess and J. Bagger, *Supersymmetry and Supergravity*, 2nd ed. (Princeton University, Princeton, NJ, 1991).

[2] H. E. Haber and G. Kane, Phys. Rep. **117**, 75 (1985); S. P. Martin, arXiv:hep-ph/9709356; D. J. H. Chung, L. L. Everett, G. L. Kane, S. F. King, J. Lykken, and L.-T. Wang Phys. Rep. **407**, 1 (2005).

[3] M. Drees, P. Roy, and R. M. Godbole, *Theory and Phenomenology of Sparticles* (World Scientific, Singapore, 2005); H. Baer and X. Tata, *Weak Scale Supersymmetry: From Superfields to Scattering Events* (Cambridge University Press, Cambridge, England, 2006).

[4] C. Jungman, M. Kamionkowski, and K. Griest, Phys. Rep. **267**, 195 (1996).

[5] G. Bertone, D. Hooper, and J. Silk, Phys. Rep. **405**, 279 (2005).

[6] T. Falk, K. A. Olive, and M. Srednicki, Phys. Lett. B **339**, 248 (1994).

[7] A. H. Chamseddine, R. Arnowitt, and P. Nath, Phys. Rev. Lett. **49**, 970 (1982); R. Barbieri, S. Ferrara, and C. A. Savoy, Phys. Lett. **119B**, 343 (1982); L. J. Hall, J. Lykken, and S. Weinberg, Phys. Rev. D **27**, 2359 (1983); P. Nath, R. Arnowitt, and A. H. Chamseddine, Nucl. Phys. **B227**, 121 (1983); N. Ohta, Prog. Theor. Phys. **70**, 542 (1983); for a review, see P. Nath, R. Arnowitt, and A. H. Chamseddine, *Applied N=1 Supergravity* (World Scientific, Singapore, 1984).

[8] The LEP SUSY Working Group, http://lepsusy.web.cern.ch/lepsusy/.

[9] U. Chattopadhyay, D. Das, A. Datta, and S. Poddar, Phys. Rev. D **76**, 055008 (2007).

[10] ATLAS Collaboration, Phys. Lett. B **716**, 1 (2012); CMS Collaboration, Phys. Lett. B **716**, 30 (2012).

[11] U. Chattopadhyay, A. Corsetti, and P. Nath, Phys. Rev. D **68**, 035005 (2003); S. Akula, M. Liu, P. Nath, and G. Peim, Phys. Lett. B **709**, 192 (2012).

[12] K. L. Chan, U. Chattopadhyay, and P. Nath, Phys. Rev. D **58**, 096004 (1998).

[13] J. L. Feng, K. T. Matchev, and T. Moroi, Phys. Rev. D **61**, 075005 (2000); Phys. Rev. Lett. **84**, 2322 (2000); J. L. Feng, K. T. Matchev, and F. Wilczek, Phys. Lett. B **482**, 388 (2000); J. L. Feng and F. Wilczek, Phys. Lett. B **631**, 170 (2005); U. Chattopadhyay, T. Ibrahim, and D. P. Roy, Phys. Rev. D **64**, 013004 (2001); U. Chattopadhyay, A. Datta, A. Datta, A. Datta, and D. P. Roy, Phys. Lett. B **493**, 127 (2000); S. P. Das, A. Datta, M. Guchait, M. Maity, and S. Mukherjee, Eur. Phys. J. C **54**, 645 (2008).

[14] H. Baer, V. Barger, and A. Mustafayev, Phys. Rev. D **85**, 075010 (2012); J. Ellis and K. A. Olive, Eur. Phys. J. C **72**, 2005 (2012); O. Buchmueller *et al.*, Eur. Phys. J. C **72**, 2243 (2012); **74**, 2922 (2014).

[15] M. Citron, J. Ellis, F. Luo, J. Marrouche, K. A. Olive, and K. J. de Vries, Phys. Rev. D **87**, 036012 (2013); K. Kowalska, L. Roszkowski, and E. M. Sessolo, J. High Energy Phys. 06 (2013) 078; S. Henrot-Versillé, R. Lafaye, T. Plehn, M. Rauch, D. Zerwas, S. Plaszczynski, B. R. d'Orfeuil, and M. Spinelli, Phys. Rev. D **89**, 055017 (2014); P. Bechtle *et al.*, *Proc. Sci.*, EPS-HEP2013 (2013) 313 [arXiv:1310.3045]; J. Ellis, Eur. Phys. J. C **74**, 2732 (2014); L. Roszkowski, E. M. Sessolo, and A. J. Williams, J. High Energy Phys. 08 (2014) 067.

[16] J. R. Ellis, K. Enqvist, D. V. Nanopoulos, and K. Tamvakis, Phys. Lett. **155B**, 381 (1985); M. Drees, Phys. Lett. **158B**, 409 (1985).

[17] A. Corsetti and P. Nath, Phys. Rev. D **64**, 125010 (2001).

[18] U. Chattopadhyay and P. Nath, Phys. Rev. D **65**, 075009 (2002).

[19] G. Anderson, C. H. Chen, J. F. Gunion, J. Lykken, T. Moroi, and Y. Yamada, arXiv:hep-ph/9609457; G. Anderson, H. Baer, C. H. Chen, P. Quintana, and X. Tata, Phys. Rev. D **61**, 095005 (2000); K. Huitu, Y. Kawamura, T. Kobayashi, and K. Puolamaki, Phys. Rev. D **61**, 035001 (1999); J. Chakrabortty and A. Raychaudhuri, Phys. Lett. B **673**, 57 (2009); S. P. Martin, Phys. Rev. D **79**, 095019 (2009).

[20] U. Chattopadhyay and D. P. Roy, Phys. Rev. D **68**, 033010 (2003).

[21] U. Chattopadhyay, A. Corsetti, and P. Nath, Phys. Rev. D **66**, 035003 (2002); U. Chattopadhyay, D. Choudhury, and D. Das, Phys. Rev. D **72**, 095015 (2005); K. Huitu, J. Laamanen, P. N. Pandita, and S. Roy, Phys. Rev. D **72**, 055013 (2005); G. Belanger, F. Boudjema, A. Cottrant, A. Pukhov, and A. Semenov, Nucl. Phys. **B706**, 411 (2005); S. F. King, J. P. Roberts, and D. P. Roy, J. High Energy Phys. 10 (2007) 106; S. Bhattacharya, A. Datta, and B. Mukhopadhyaya, J. High Energy Phys. 10 (2007) 080; K. Huitu, R. Kinnunen, J. Laamanen, S. Lehti, S. Roy, and T. Salminen, Eur. Phys. J. C **58**, 591 (2008); S. Bhattacharya and J. Chakrabortty, Phys. Rev. D **81**, 015007 (2010).

[22] U. Chattopadhyay, D. Das, and D. P. Roy, Phys. Rev. D **79**, 095013 (2009).

[23] M. Guchait, D. P. Roy, and D. Sengupta, Phys. Rev. D **85**, 035024 (2012); S. Mohanty, S. Rao, and D. P. Roy, J. High Energy Phys. 11 (2012) 175; 09 (2013) 027; J. Chakrabortty, S. Mohanty, and S. Rao, J. High Energy Phys. 02 (2014) 074; S. P. Martin, Phys. Rev. D **89**, 035011 (2014); S. P. Das, M. Guchait, and D. P. Roy, Phys. Rev. D **90**, 055011 (2014); I. Gogoladze, F. Nasir, Q. Shafi, and C. S. Un, Phys. Rev. D **90**, 035008 (2014)

[24] U. Chattopadhyay, D. Choudhury, M. Drees, P. Konar, and D. P. Roy, Phys. Lett. B **632**, 114 (2006).

[25] A. Kaminska, G. G. Ross, and K. Schmidt-Hoberg, J. High Energy Phys. 11 (2013) 209; K. Kowalska, L. Roszkowski, E. M. Sessolo, and S. Trojanowski, J. High Energy Phys. 04 (2014) 166.

[26] S. Komine and M. Yamaguchi, Phys. Rev. D **63**, 035005 (2001).

[27] A. Djouadi, J.-L. Kneur, and G. Moultaka, Comput. Phys. Commun. **176**, 426 (2007).

[28] T. Hahn, S. Heinemeyer, W. Hollik, H. Rzehak, and G. Weiglein, Comput. Phys. Commun. **180**, 1426 (2009).

[29] G. Degrassi, S. Heinemeyer, W. Hollik, P. Slavich, and G. Weiglein, Eur. Phys. J. C **28**, 133 (2003); B. C. Allanach, A. Djouadi, J. L. Kneur, W. Porod, and P. Slavich, J. High Energy Phys. 09 (2004) 044; S. P. Martin, Phys. Rev. D **75**, 055005 (2007); R. V. Harlander, P. Kant, L. Mihaila, and M. Steinhauser, Phys. Rev. Lett. **100**, 191602 (2008); **101**, 039901 (2008); S. Heinemeyer, O. Stal, and G. Weiglein, Phys. Lett. B **710**, 201 (2012); A. Arbey, M. Battaglia, A. Djouadi, and F. Mahmoudi, J. High Energy Phys. 09 (2012) 107.

[30] See, for example, the following and references therein: U. Chattopadhyay and A. Dey, J. High Energy Phys. 11 (2014) 161.

[31] R. Aaij *et al.* (LHCb Collaboration), Phys. Rev. Lett. **111**, 101805 (2013).

[32] S. Chatrchyan *et al.* (CMS Collaboration), Phys. Rev. Lett. **111**, 101804 (2013).

[33] CMS and LHCb Collaborations, Report No. CMS-PAS-BPH-13-007.

[34] D. Feldman, Z. Liu, and P. Nath, Phys. Rev. D **81**, 117701 (2010); S. Akula, D. Feldman, P. Nath, and G. Peim, Phys. Rev. D **84**, 115011 (2011).

[35] Y. Amhis *et al.* (Heavy Flavor Averaging Group Collaboration), arXiv:1207.1158.

[36] For discussions on BR$(B \to X_s\gamma)$ a partial list is as follows: B. Bhattacherjee, M. Chakraborti, A. Chakraborty, U. Chattopadhyay, D. Das, and D. K. Ghosh, Phys. Rev. D **88**, 035011 (2013); U. Haisch and F. Mahmoudi, J. High Energy Phys. 01 (2013) 061; N. Chen, D. Feldman, Z. Liu, and P. Nath, Phys. Lett. B **685**, 174 (2010); M. E. Gomez, T. Ibrahim, P. Nath, and S. Skadhauge, Phys. Rev. D **74**, 015015 (2006); U. Chattopadhyay and P. Nath, Phys. Rev. D **65**, 075009 (2002).

[37] G. Hinshaw *et al.* (WMAP Collaboration), Astrophys. J. Suppl. Ser. **208**, 19 (2013).

[38] P. A. R. Ade *et al.* (Planck Collaboration), Astron. Astrophys. **571**, A16 (2014).

[39] A. Sailer, Eur. Phys. J. Web Conf. **70**, 00085 (2014).

[40] R. L. Arnowitt and P. Nath, Phys. Rev. D **46**, 3981 (1992).

[41] W. Beenakker, R. Hopker, M. Spira, and P. M. Zerwas, Nucl. Phys. **B492**, 51 (1997); W. Beenakker, R. Hopker, and M. Spira, arXiv:hep-ph/9611232.

[42] H. Baer, V. Barger, A. Lessa, and X. Tata, Phys. Rev. D **86**, 117701 (2012).

[43] A. Djouadi, M. M. Muhlleitner, and M. Spira, Acta Phys. Pol. B **38**, 635 (2007).

[44] V. Barger, W. Y. Keung, and B. Yencho, Phys. Lett. B **687**, 70 (2010); V. Khachatryan *et al.* (CMS Collaboration), J. High Energy Phys. 11 (2014) 154; J. Keaveney, arXiv:1412.4641.

[45] J. Hisano, S. Matsumoto, M. M. Nojiri, and O. Saito, Phys. Rev. D **71**, 015007 (2005).

[46] G. Belanger, F. Boudjema, A. Pukhov, and A. Semenov, Comput. Phys. Commun. **185**, 960 (2014).

[47] E. Aprile *et al.* (XENON100 Collaboration), Phys. Rev. Lett. **109**, 181301 (2012).

[48] D. S. Akerib *et al.* (LUX Collaboration), Phys. Rev. Lett. **112**, 091303 (2014).
[49] E. Aprile *et al.* (XENON1T Collaboration), Springer Proc. Phys. **148**, 93 (2013).
[50] V. Barger, W. Y. Keung, and G. Shaughnessy, Phys. Rev. D **78**, 056007 (2008).
[51] M. G. Aartsen *et al.* (IceCube Collaboration), Phys. Rev. Lett. **110**, 131302 (2013).
[52] R. Abbasi *et al.* (IceCube Collaboration), Phys. Rev. D **85**, 042002 (2012).
[53] P. Cushman *et al.*, arXiv:1310.8327.
[54] E. Behnke *et al.* (COUPP Collaboration), Phys. Rev. D **86**, 052001 (2012).
[55] M. Ackermann *et al.* (Fermi-LAT Collaboration), Phys. Rev. Lett. **107**, 241302 (2011).
[56] A. Ibarra, M. Totzauer, and S. Wild, J. Cosmol. Astropart. Phys. 04 (2014) 012.
[57] A. Gould, Astrophys. J. **321**, 560 (1987); **321**, 571 (1987).
[58] K. Griest and D. Seckel, Nucl. Phys. **B283**, 681 (1987); **B296**, 1034(E) (1988).
[59] J. Buckley *et al.*, arXiv:1310.7040.
[60] G. Wikstrom and J. Edsjo, J. Cosmol. Astropart. Phys. 04 (2009) 009.
[61] P. Agrawal, Z. Chacko, C. Kilic, and R. K. Mishra, arXiv:1003.5905.